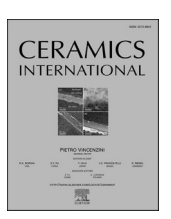
ELSEVIER

Contents lists available at ScienceDirect

Ceramics International

journal homepage: www.elsevier.com/locate/ceramint





Effect of in-situ NbC content on the microstructure and mechanical properties of Ni625 composite coating by laser cladding

Yingying Zhang, Tianbiao Yu^{*}, Jiayu Sun, Zhengyu Sun, Yiqi Wang

School of Mechanical Engineering and Automation, Northeastern University, Shenyang, 110819, China

ARTICLE INFO

Handling Editor: Dr P. Vincenzini

Keywords: In-situ NbC Laser cladding Microhardness Wear resistance Corrosion resistance

ABSTRACT

To improve the mechanical properties of Ni625 coatings, different contents of Nb powder and Ni-coated graphite particles were added to Ni625 powder for in-situ generation of NbC particles. The effects of different NbC contents on the microstructure, hardness, wear resistance and corrosion resistance of Ni625 coatings were investigated. The results show that the highest XRD phase diffraction peaks of NbC in the coating are obtained with the addition of 15 % (Nb 9.9 %, Ni-coated graphite particles 5.1 %), and the coating exhibits a hardness of 441.9 HV, which is 1.53 times greater than that of the coating with the addition of 0 %. Furthermore, the wear coefficient (μ) of the coating is 0.4804, and the wear volume is 0.0042 mm³, representing a reduction of 23.5 % and 64.1 %, respectively, in comparison to the coating with 0 % additive. However, the coating with an addition of 20 % does not generate more NbC phase, and the hardness and wear resistance are not further improved. The coating with an addition of 10 % has the best corrosion resistance, with a corrosion current density of 2.1829E-10 A/cm². Further additions do not result in an enhanced corrosion resistance of the coating. Therefore, appropriate amount of in-situ generation of NbC within the Ni625 coating during the laser cladding process can effectively enhance the mechanical properties of the Ni625 coating.

1. Introduction

Laser cladding (LC) is a highly efficient surface treatment technology that is widely used due to its ability to rapidly melt and solidify the cladding powder on the substrate. The coatings prepared by this process have the advantages of fine particle size and durability, low dilution and small heat-affected zone, environmental friendliness, flexibility, and high material utilization efficiency [1,2]. Ni625, as a nickel-based high-temperature alloy, is widely used in aerospace, petrochemical, and shipbuilding applications due to its high yield strength, excellent oxidation and corrosion resistance, and superior tensile strength to other nickel-based alloys [3,4]. Scholars use LC to prepare nickel-based alloy coatings with different reinforcing phases to improve their mechanical properties [5–7]. Nb is an ideal element for solid solution strengthening of high-temperature alloys, which can enhance the homogeneity of the coating and the mechanical properties of high-temperature alloys [8–10]. Cheng et al. [11] investigated Ni-based niobium carbide (NbC) coatings and found that the addition of 20 % NbC improved the hardness, wear and corrosion resistance of the coatings and provided a better protective barrier for AISI 4145H steel with high resistance to passivation, low corrosion currents and positive corrosion potential. Yufan et al. [12] investigated the effect of process parameters and NbC additions on Ni-based alloy coatings, and found that the coating has the optimal wear resistance at a 6 wt% NbC addition. However, a further increase in NbC addition resulted in a decrease in the wear resistance of the coating.

However, composite materials are limited by the weak bonding and poor wettability between the reinforcing phase and the original matrix. Therefore, in-situ generation technology has been gradually promoted in the manufacture of composite coatings [13,14]. Zhang et al. [15] deposited iron-based alloy coatings without NbC addition, coatings with NbC addition, and reinforced composite coatings with in-situ generated NbC on SS304. The results showed that the in situ-generated NbC coatings exhibited superior performance in grain refinement, microhardness, wear resistance and corrosion resistance due to the uniform dispersion of the reinforcements and the formation of protective passivation films. Zhang et al. [16] investigated the influence of scanning rate and laser power on the microstructure, wear, and corrosion resistance of the in-situ generated WC-reinforced Ni-based coatings. The results indicated that the in-situ WC phase significantly increased the

E-mail address: tianbiaoyudyx@gmail.com (T. Yu).

^{*} Corresponding author.

microhardness of the coatings and that the laser power played a crucial role in improving the wear and corrosion resistance. Xi et al. [17] improved the wear resistance of Fe-based cladding by generating NbC particles in-situ with different morphologies, finding that cross-shaped NbC particles, formed by adding specific amounts of Nb, Cr₃C₂, and C, provide the best wear resistance. Shi et al. [18] used plasma spray welding to create an in-situ NbC reinforced Ni-based composite coating on low carbon steel, achieving optimal microhardness (1025 HV) and wear resistance with 20 % Nb + NiCr-Cr₃C₂ addition. Liu et al. [19] indicated that in-situ NbC-reinforced Ni45 coatings synthesized using cost-effective FeNb65 and Cr_3C_2 exhibited excellent microhardness (776.3 HV) and abrasion resistance, making them well suited for surface strengthening and repair applications. Wang et al. [20] found that refining in-situ NbC in Cu-matrix composites resulted in a 1320 % increase in the oxidation products (NbO₂, NB₂O₅), which improved the corrosion resistance due to the protective effect of the oxides without changing the corrosion mechanism. Zhao et al. [21] used in-situ TiC and (Ti, Nb)C particles to enhance Ni204-based composite coatings via laser cladding, achieving a 1.53-fold increase in microhardness and 11-fold improvement in wear resistance by optimizing the Ti/C/NbC ratio. Zhang et al. [22] improved Mo₂FeB₂ coatings by adding in-situ synthesized NbC, WC, and TaC via laser cladding, with the Mo2FeB2/WC composite showing the highest microhardness (1543.6 HV) and superior wear resistance. Lian et al. [23] prepared NbC-enhanced Ni-based coatings by laser cladding and found that increasing the B₄C content could increase the hardness of the coatings (up to 1794.1 HV), with abrasive wear being the main wear mechanism. Chen et al. [24] fabricated in-situ NbC reinforced Fe-based coatings on medium carbon steel by laser cladding, and the results showed that the addition of Nb and B₄C powders significantly increased the hardness (866.36 HV) and wear resistance, which changed the wear mechanism of the coating from abrasive wear to adhesive wear. Gaddam et al. [25] used direct laser deposition to prepare a composite containing 90 wt% Ni and 10 wt% NbC, and formed a complex hierarchical microstructure consisting of primary dendritic Ni-rich γ phase and interdendritic γ + NbC eutectic, which further decomposed into a lamellar $\gamma + \delta$ phase (Ni₃Nb). Wang et al. [26] investigated the effect of varying laser power levels on the microstructure and corrosion resistance of Ni-based alloy coatings prepared on ductile iron via high-speed laser cladding, and found that increasing the laser power improved both the chemical homogeneity and the corrosion resistance of the coatings. Liang et al. [27] studied the effects of Y2O3 additives on Ni-based/WC coatings fabricated on 316L stainless steel, and the results showed that the addition of Y₂O₃ could effectively refine the microstructure of the coatings, increase the microhardness, and significantly improve the corrosion and wear resistance in marine environments. Wang et al. [28] applied the underwater wet laser cladding technique to clad 316L stainless steel with an in-situ Ni interlayer on EH40, and found that the interlayer improved the microhardness, wear, and corrosion resistance of the coatings by forming a diffusion buffer, thereby improving its performance to levels comparable to in-air cladding. Yao et al. [29] investigated the impact of laser power on Ni-based alloy coatings applied to 30CrMnSiA steel, and showed that, due to finer grains and less elemental dilution, lower laser power could improve the microhardness and corrosion resistance of the coatings, with 2400 W providing the best performance.

Although previous studies have shown that the in-situ generation of NbC can be used to improve the mechanical properties of the coatings, the effect of NbC on the mechanical properties and corrosion resistance of the coatings, and the optimal amount of NbC to be added have not been fully investigated. Therefore, in this study, the laser cladding technique was used to generate NbC in situ by adding five ratios of Nb powder and Ni-coated graphite particles to Ni625 powder to improve the mechanical properties and corrosion resistance of the coatings and to obtain the optimum amount of additive. The results show that the appropriate amount of in-situ NbC significantly improves the performance of the coatings, and the coatings exhibit the best mechanical

properties when the addition amount is 15 %, with a hardness of 441.9 HV, which is 1.53 times higher than that of the no additive layer. The wear volume was $0.0042~\mathrm{mm}^3$, which was 64.1 % lower than that of the no additive layer. In addition, the coating with 10 % addition has the best corrosion resistance and the lowest corrosion current density of $2.1829\mathrm{E}\text{-}10~\mathrm{A/cm}^2$. This study systematically and comprehensively reveals the effects of different in-situ NbC contents on the mechanical properties and corrosion resistance of Ni625 coatings, providing a theoretical basis and technical support for practical applications.

2. Materials and methods

2.1. Materials and equipment

The deposition materials consist of spherical Ni625 powder (average particle size 84.3 µm), spherical Nb powder with a purity of 99.9 % (average particle size $50.78 \, \mu m$), and Ni-coated graphite particles with a purity of 99.95 % (average length 23.64 μ m). The mass ratio of Ni and C in the Ni-coated graphite particles is 3:1. The elemental composition of the spherical Ni625 powder was 0.023 wt% C, 21.1 wt% Cr, 9.04 wt% Mo, 3.63 wt% Nb, 0.036 wt% Fe, 0.018 wt% Si, with the remainder being Ni. The SEM morphologies and size distributions of the Ni625 powder, Nb, and Ni-coated graphite particles are presented in Fig. 1. To gradually increase the in-situ NbC particles in the composite coating, five types of composite powders were designed based on the atomic ratio of Nb and C in the Nb + C \rightarrow NbC chemical reaction. The mass fractions of the elements are listed in Table 1. The composite powders were thoroughly mixed by ball milling at a speed of 450 r/min for 40 min. The mass ratio of alumina balls to powder was 2:1. Subsequently, the mixture was sieved using a 100-mesh screen to remove impurities, and then dried in an oven for 1 h to remove moisture. The substrate was a 42CrMo steel plate (100 mm \times 100 mm \times 10 mm), which was cleaned with alcohol to remove surface stains before use.

The experiment used a coaxial powder-feeding laser cladding system consisting of a control system, a powder-feeding mechanism, and a Kuka robot, as shown in Fig. 1. The spot diameter was 1 mm. The main parameters are as follows: laser power of 450 W, scanning rate of 9 mm/s, powder feed rate of 10.21 g/min, track spacing of 0.73 mm, and Z-axis increment of 0.18 mm. Both the powder feeder and the shielding gas system utilized 99.99 % pure argon, with flow rates of 8 L/min and 15 L/min, respectively.

2.2. Process and characterization

After laser cladding, the samples were cut using electrical discharge machining. The cutting method and sample dimensions are shown in Fig. 2. Each sample was divided into three parts: one part for friction-wear testing and XRD analysis, one part for hardness testing and SEM analysis, and one part for electrochemical corrosion testing.

The test surfaces of the samples were ground and polished with sandpaper and then etched by aqua regia. The microstructure was observed using a LEXT OLS4100 3D microscope. The microstructure and elemental characteristics of the materials were obtained by Zeiss Ultra PLUS scanning electron microscope. The phase analysis of the samples was carried out using Rigaku SmartLab. The hardness analysis of the samples was carried out using an MH-500 microhardness tester. The friction and wear tests were carried out using MFT-4000 multifunctional material surface performance tester. The electrochemical tests were carried out using Gamry reference 600, and the quasi-steady-state values of the open circuit potential (OCP) were obtained by placing the coldinserted samples with a contact area of 0.25 cm2 in 3.5 wt% NaCl solution for 30 min. The potentiodynamic tests were carried out in the range of 0.5 V–1.5 V with a scan rate of 1 mV/s. The electrochemical impedance spectroscopy (EIS) measurements were carried out in the frequency range of 100 kHz to 100 mHz with an AC amplitude of 10 mV/ OCP.

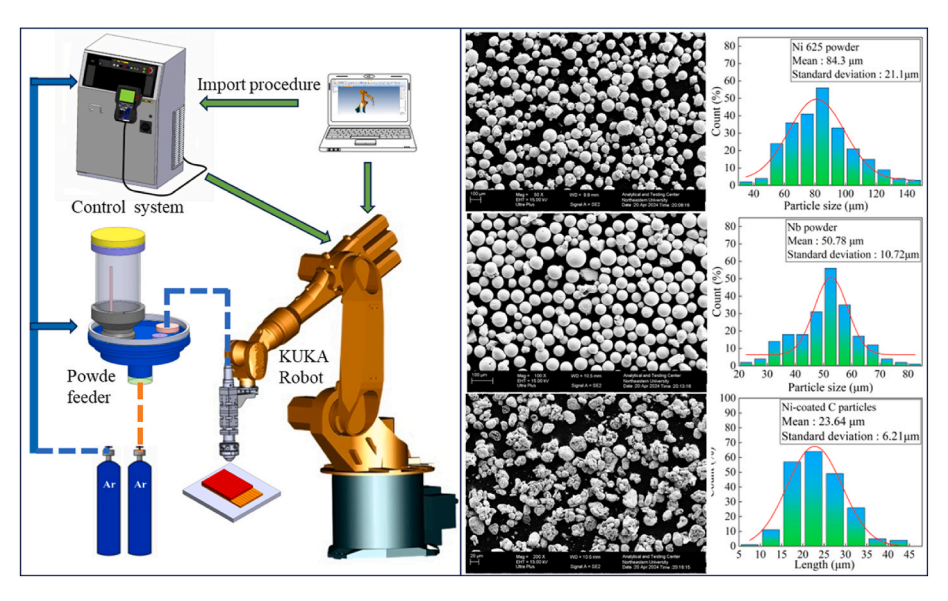


Fig. 1. Preparation process of in-situ NbC and morphology of deposited materials.

Table 1Mass fraction of five composite powders.

No.	Powder (wt%)				
	Ni625	Nb	Ni-coated graphite particles		
S1	100	0.00	0.00		
S2	95	3.30	1.70		
S3	90	6.60	3.40		
S4	85	9.90	5.10		
S5	80	13.20	6.80		

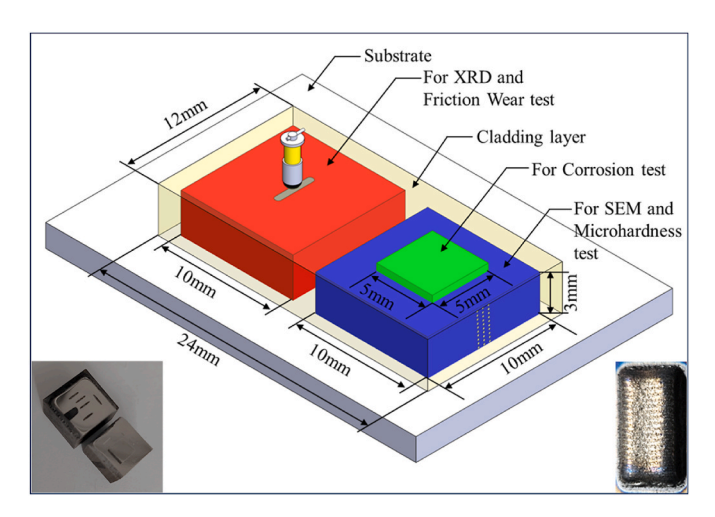


Fig. 2. Sample cutting method and size.

3. Results and discussion

3.1. Microstructure

3.1.1. Phase composition

Fig. 3 presents the XRD spectra and NbC content of five coatings. As indicated in the figure, without Nb and Ni-coated graphite particles, the S1 coating is primarily composed of the FCC structure of Ni625 and $\gamma\textsc{-Ni}$ phase solid solutions. The presence of NbC diffraction peaks in the S2-S5 coatings indicates that the NbC phase was in-situ synthesized during the laser cladding process. This finding is consistent with the relationship

between the Gibbs free energy of the in-situ synthesis reaction and temperature, as previously reported in Ref. [30]. As the quantity of added Nb and Ni-coated graphite particles increased in S2-S4 coatings, the amount of NbC rose. However, in S5, the amount of NbC decreased and was comparable to that of S3. The highest NbC diffraction peaks were observed in S4, and the highest amount of NbC was found in S4.

3.1.2. SEM characterization

Fig. 4 presents the EDS spectrum at 10.00 KX magnification. As illustrated in the figure, the surface of the Ni625 laser cladding coating (S1) exhibits a prominent cellular crystal structure. The addition of Nb and Ni-coated graphite particles resulted in the formation of bright, lumpy precipitates which comprises Cr, Mo, and Nb elements. In light of the XRD results, it can be concluded that these precipitates are in-situ generated NbC phases. As the in-situ generated NbC phase increases gradually, the lattice distortion is further exacerbated. The precipitates of NbC in coatings (S2 to S4) increase in both size and number and their formation occurs along the grain boundaries. It is noteworthy that in the S5 sample, the massive precipitates become denser but decrease in size.

Fig. 5 presents the EDS spectra at a magnification of 2.00 KX, while Table 2 lists the elemental compositions at magnifications of 2.00 KX and 10.00 KX. It is observed that with the increase of the addition of Nb and Ni-coated graphite particles, the Nb content in samples S2 to S4 increases gradually, with the highest Nb content in S4, and then decreases in S5. Notably, the Nb distribution in S1 to S4 is more uniform compared to that in S5. There is no obvious difference in the distribution of O, Cr, and Fe elements among the five coatings. The C content is lowest in S2, which correlates with the minimal addition of Ni-coated graphite particles in this sample. Due to the low density of the Nicoated graphite particles, a small portion was likely blown away by the powder feeding gas and protective gas during the laser cladding process, and the C from Ni625 also participated in the in-situ reaction with NbC. The content of Ni and Mo is the lowest in S4, where the powder ratio led to the highest amount of in-situ NbC phase. Interestingly, sample S5 has the highest incorporation of Nb and Ni-coated graphite particles, but as can be seen from the XRD results in Fig. 3, the NbC diffraction peaks in this sample are not high. As a result, the NbC phase formation was not maximized. This phenomenon can be attributed to the supersaturation of Nb and C, as their addition exceeds a certain threshold. Excess Nb and C might not completely dissolve in the melt pool, and the laser power might be insufficient to sustain the in-situ reaction. Additionally, some unreacted powders might be blown away by the powder-feeding gas and protective gas, leading to a

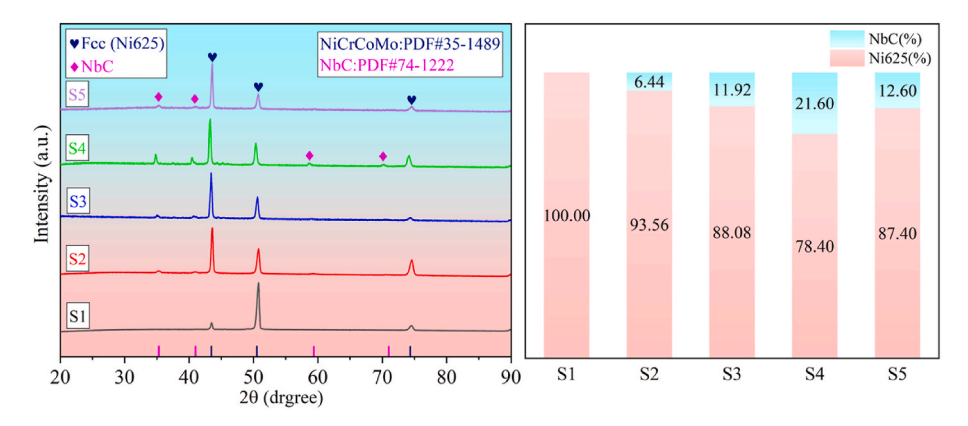


Fig. 3. XRD patterns of five coatings and their corresponding NbC content.

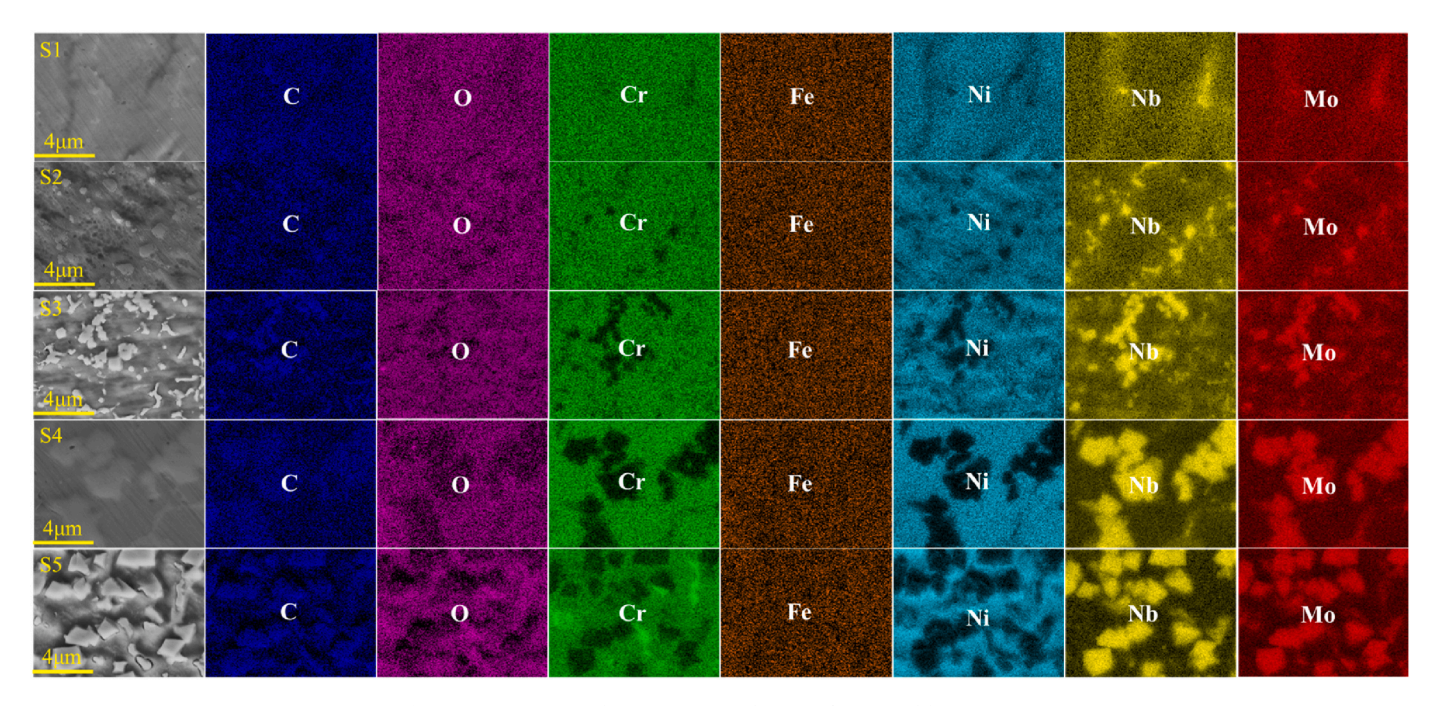


Fig. 4. EDS mapping of 10.00 KX magnification elements of five coatings.

disproportionate relationship between the in-situ synthesized NbC in S5 and the amount of Nb and Ni-coated graphite particle added.

3.2. Mechanical properties

3.2.1. Microhardness

Fig. 6 illustrates the mean microhardness of five coatings. As the insitu synthesized NbC increases, the microhardness of the coating also increases accordingly. In particular, the microhardness of S4 reaches the maximum value of 441.9 HV, which is approximately 1.53 times that of S1 (Ni625 coating). In accordance with the classical Fleischer theory [15], notable discrepancies in atomic radius lead to increased resilience against dislocation movement and lattice distortion. This mechanism explains why the material hardness increases and grain refinement occurs as a result of the in-situ synthesized NbC. The mean hardness curves for S1-S4 are relatively smooth with minimal fluctuations, indicating a uniform hardness distribution and an even dispersion of the NbC phase. In contrast, the hardness curve for S5 exhibits obvious fluctuations, initially displaying a relatively low value and then a markedly higher one, indicating a non-uniform hardness distribution.

Fig. 7 illustrates the hardness indentation plots of the five coatings at a distance of $1200 \mu m$ from the substrate. From the figure, it can be seen

that the microstructures around the indentations of S1-S4 are uniformly distributed. As the addition of Nb and Ni-coated graphite particles increases, hardness gradually improves, grains become more refined, and the indentation diagonal decreases accordingly. However, the microstructure around the S5 indentation seems to be not uniform enough, which contributes to the large fluctuation in S5 hardness values. It is worth noting that the relationship between hardness values and the amount of addition is not linear. This observation is consistent with the XRD and SEM results, which indicate that the Nb and Ni-coated graphite particles in the coatings have reached a critical value, leading to the limit of the solvation and generation capacity of Ni625 powder, which led to a non-uniform distribution of in situ-generated NbC and ultimately resulted in the fluctuating hardness of S5.

3.2.2. Wear resistance

Fig. 8 illustrates the COF-time curves of five different coatings. Initially, all the samples (S1-S5) showed different levels of variation in their coefficient of friction (COF). This is attributable to the limited plastic deformation of the polished surface and the restricted contact area with the Si3N4 counter ball. As the area of plastic deformation increases, shear blocks, and delamination layers are formed. The coefficient of friction for all samples reached a stable stage after

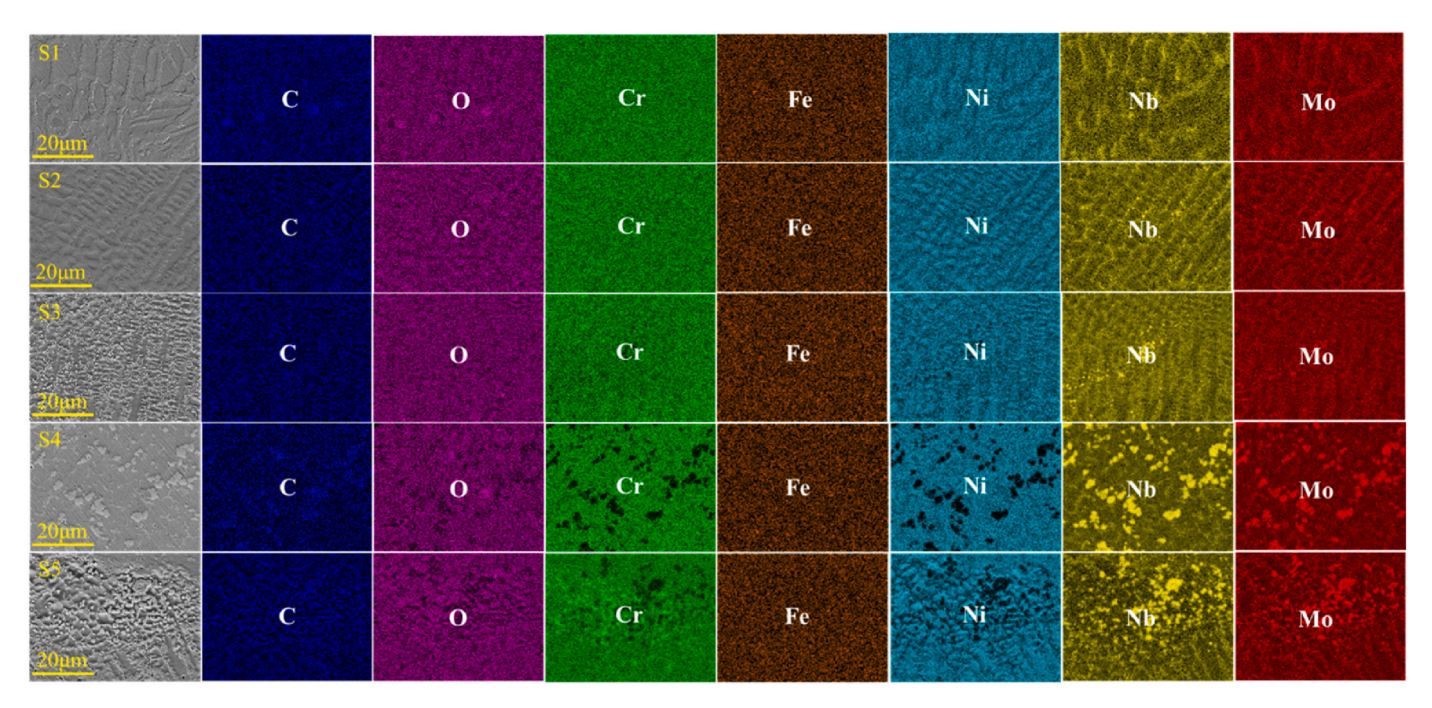


Fig. 5. EDS mapping of elements at 2.00 KX magnification of five coatings.

 Table 2

 Energy spectrum composition table of five coatings.

No.	Element (At%)							Magnification
	С	0	Cr	Fe	Ni	Nb	Мо	
S1	23.11	1.37	19.81	1.09	49.89	1.37	3.37	2.00 K X
S2	17.91	1.77	20.57	1.23	52	2.96	3.56	
S3	18.76	1.37	19.47	1.19	50.47	5.29	3.45	
S4	20.92	1.59	17.96	1.04	47.18	8.34	2.96	
S5	21.41	1.49	19.57	1.08	47.69	5.03	3.73	
S1	24.39	1.06	19.46	1.12	49.25	1.41	3.31	10.00 K X
S2	18.63	1.49	20.31	1.2	50.99	3.68	3.7	
S3	21.8	1.45	17.67	1.07	47.29	7.65	3.07	
S4	27.68	1.86	14.93	0.91	38.29	13.58	2.76	
S5	27.61	1.25	17.27	0.9	39.46	9.47	4.04	

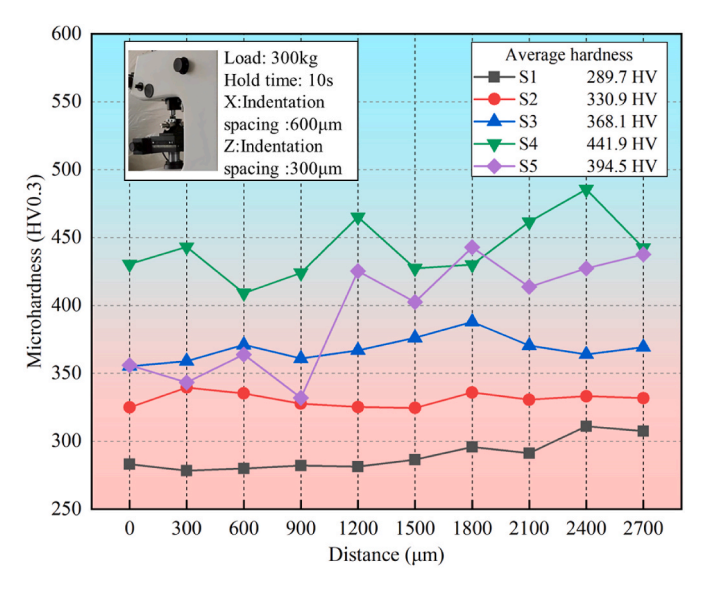


Fig. 6. Microhardness of five coatings.

approximately 15 min. The mean COF values were calculated using the data from the final 10 min of the test period, and the following results were obtained: The mean μ values of the samples are as follows: $S1\mu=0.6278,\,S2\mu=0.5750,\,S3\mu=0.5582,\,S4\mu=0.4804,$ and $S5\mu=0.5105.$ The lowest COF was observed in S4, exhibiting a 23.5 % reduction compared to S1 (Ni625 coating).

Fig. 9 illustrates the 3D wear track and depth profiles. The wear behavior of S1 indicates that due to its low microhardness, edge deformation is significant during the wear process, resulting in the deepest wear track. The wear profile of S2 is characterized by being deeper at both ends and shallower in the center, indicating higher stress at the end during the wear process. In contrast, S3 exhibits the opposite pattern with lighter ends and a deeper center, indicating higher wear forces in the central region. The depth of interfacial wear for S3 is deeper than that of S2, which may be attributed to the distribution of forces. Of all the samples, S4 exhibits the finest wear track and the shallowest wear depth, indicating excellent wear resistance. This may be attributed to the fact that S4 had the highest microhardness and a more homogeneous coating structure that resists wear effectively. Although S5 had the highest addition of Nb and Ni-coated graphite particles, its wear track was not as fine and its wear depth was not as shallow as that of S4.

Fig. 10 illustrates the wear morphology and volume loss of the five coatings. The surfaces of all five coatings exhibit the hallmarks of

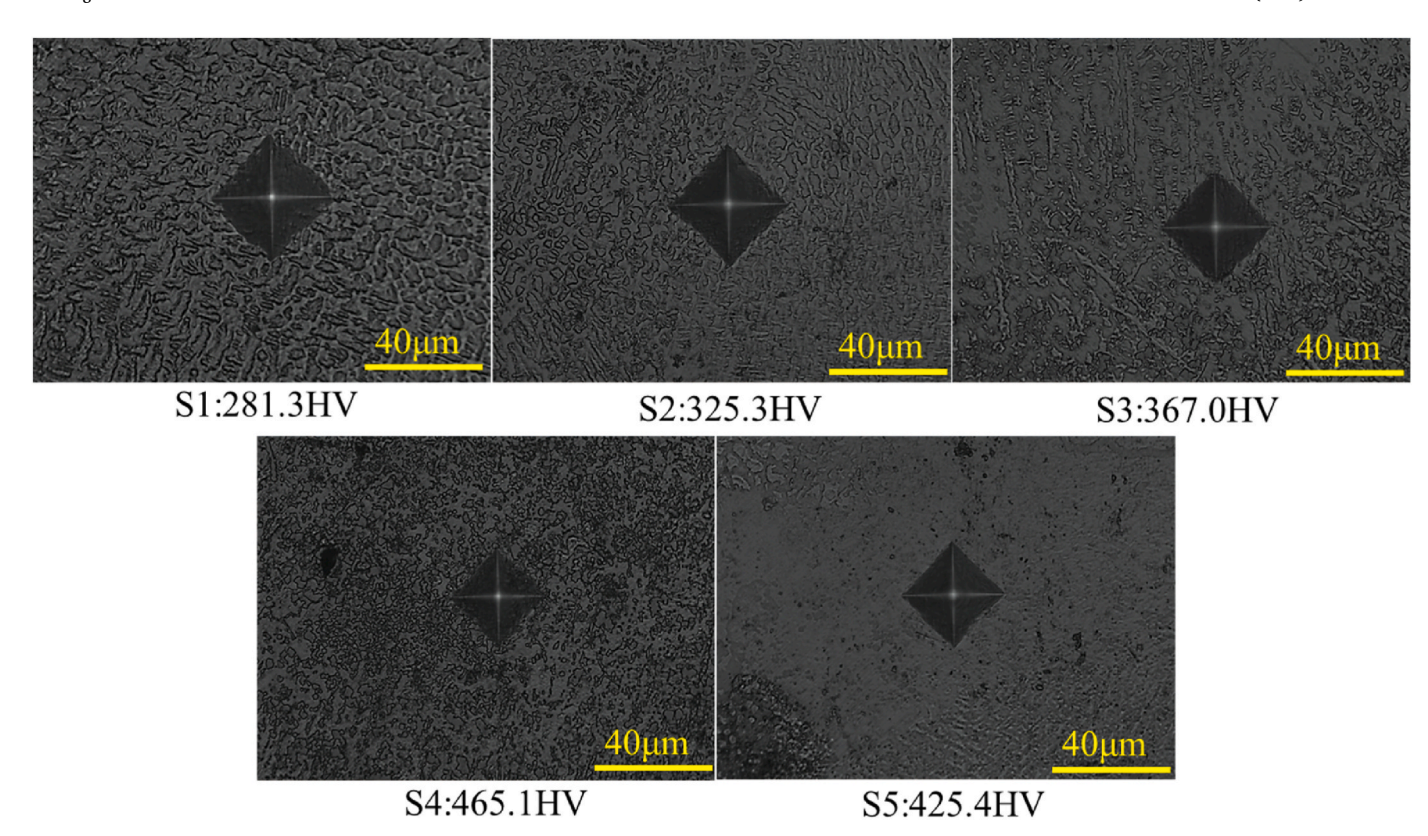


Fig. 7. Indentation images of five coatings.

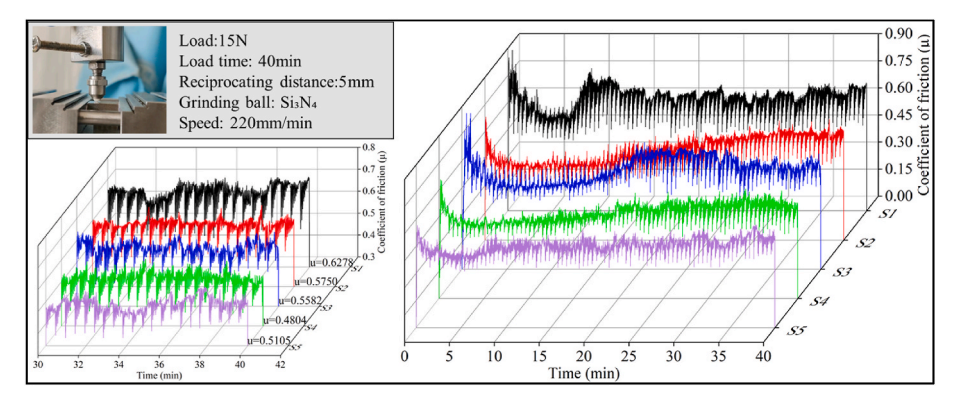


Fig. 8. COF vs time curves of five coatings.

adhesive wear, characterized by ploughing, adhesion phenomena, and spalling. The worn surface of S1 displays particularly pronounced ploughing and adhesion, accompanied by significant spalling. These observations indicate that the S1 coating was subjected to a significant shear stress during friction, resulting in material removal and deformation. The volume loss of the S1 coating was the largest, at 0.0117 mm³, indicating that the wear resistance of S1 was the poorest. The worn surface of S2 also exhibited ploughing and adhesion characteristics, but with a reduction in the number of areas of flaking, indicating an enhancement in the wear resistance. The worn surface of S3 exhibited not only ploughing and adhesion but also flaking and spalling, indicating that the local stress concentration was evident during the wear process, which led to local failure of the coating material. Although the volume loss of S3 is higher than that of S2, its COF is lower. This may be attributed to the in-situ synthesized NbC phase providing superior lubrication during the wear process, thereby reducing the COF. The worn surface of S4 displays extensive spalling and adhesion, indicating excellent wear resistance with minimal flaking. The volume loss of the

S4 coating is the lowest, at 0.0042 mm³, which is 64.1 % lower than that of S1 coating. The worn surface of S5 displays clear evidence of ploughing, adhesion, and spalling, yet exhibits minimal flaking. Despite the highest addition of Nb and Ni-coated graphite particles, S5 does not achieve the lowest COF or volume loss, which is consistent with the fact that it does not have the highest microhardness. Previous research has also demonstrated that when NbC was directly added in amounts exceeding 20 %, NbC aggregates formed, leading to the presence of pores and cracks within the coating. These structural defects can be identified as factors that prevented a reduction in the coefficient of friction (COF) [11]. This suggests that the addition of 15 % Nb and Ni-coated graphite particles (S4) can effectively enhance the wear resistance of the laser coatings, while excessive addition does not improve these properties.

3.2.3. Corrosion resistance

Fig. 11(a) and (b) are the Nyquist and Bode diagrams of the coatings, and Fig. 11(d) is the equivalent fitting circuit. As shown in Fig. 11(a), the

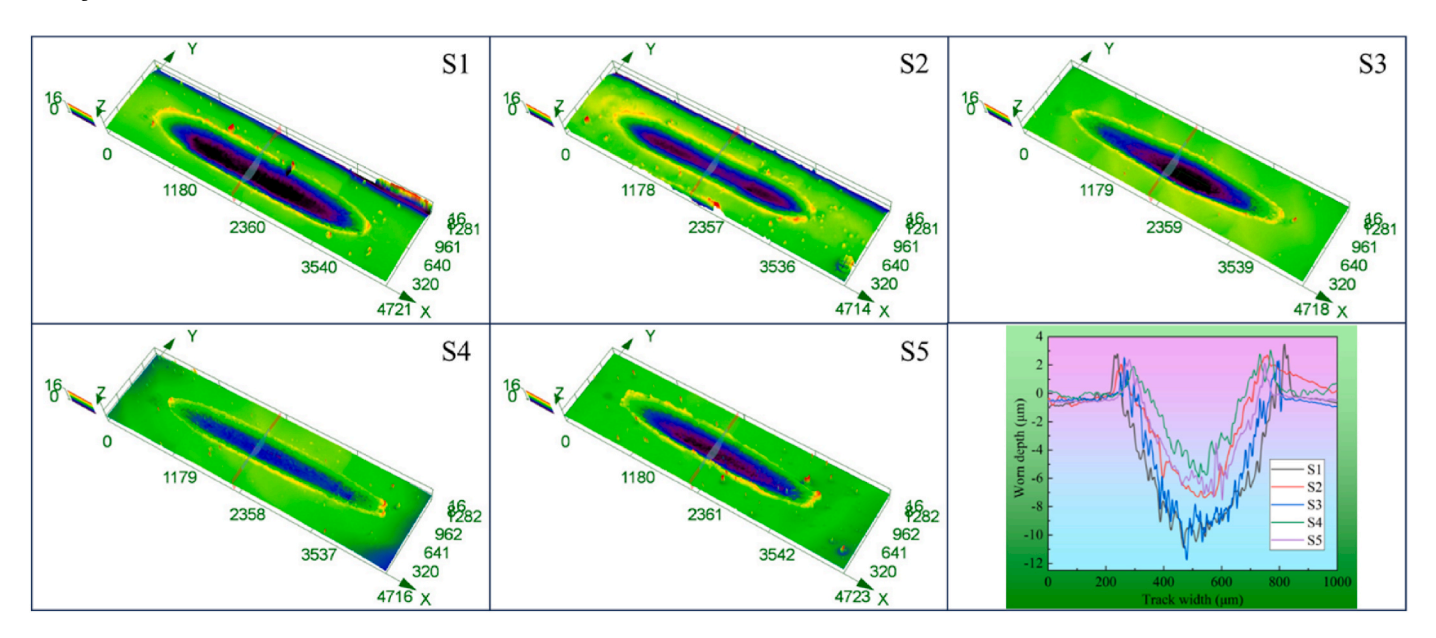


Fig. 9. 3D wear track map and scratch depth chart.

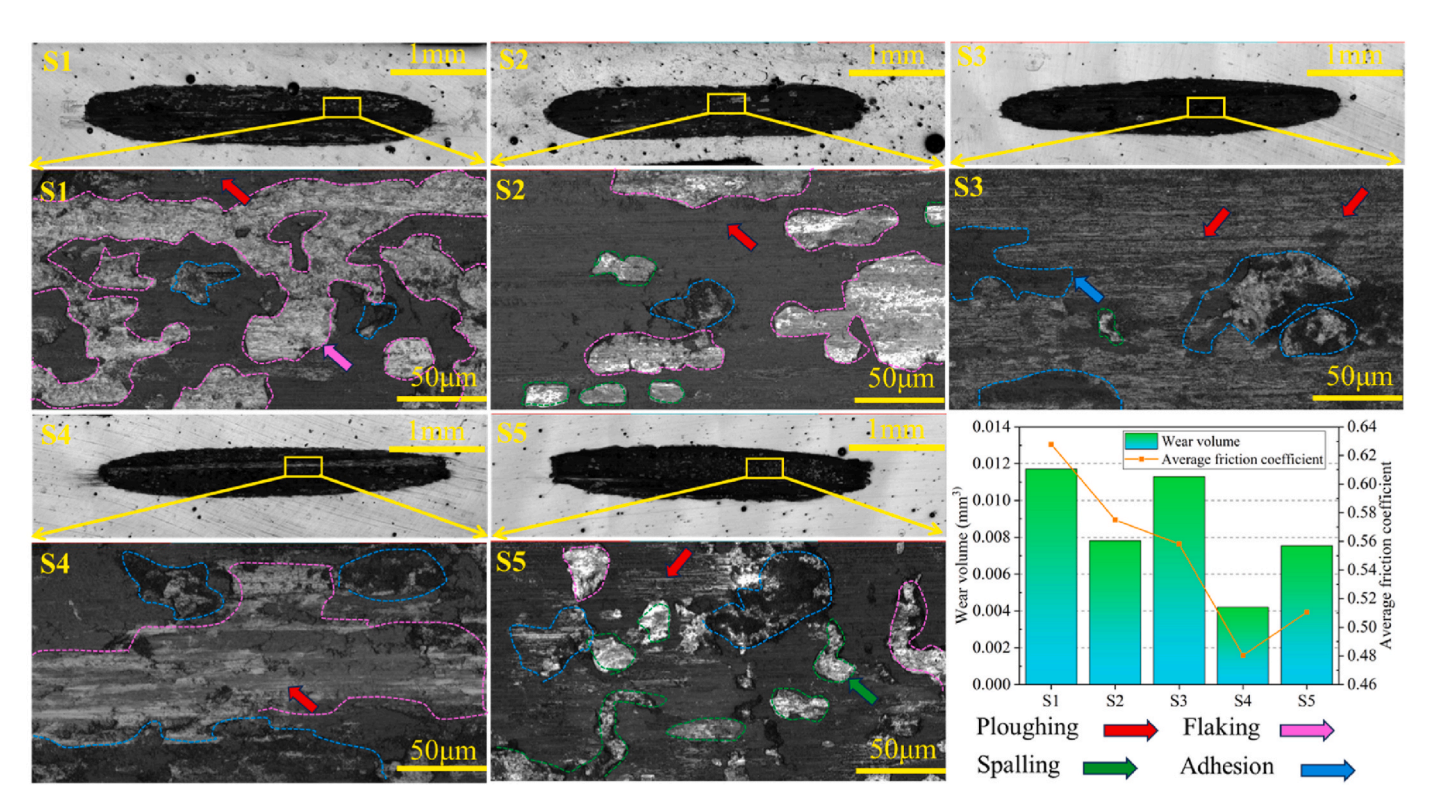


Fig. 10. Wear morphologies of five coatings and volume loss chart.

curves for S4 and S5 are positioned closer to the origin and exhibit smaller radii, indicating that the charge transfer resistance is low, the chemical reaction rate is fast, and the corrosion resistance is poor. The S3 curve is the most distant from the origin and displays a larger radius, indicating superior charge transfer resistance, reflecting better corrosion resistance.

As shown in Fig. 11(b), it is observed that the impedance modulus of S3 is the highest in the low-frequency region, demonstrating superior impedance characteristics. The impedance modulus of S1 and S2 are slightly lower than that of S3. The impedance modulus of S4 is unstable in the low-frequency region, with no data being displayed within the

coordinate range. This instability may result from oscillatory fluctuations caused by increased bubble formation during the experiment. The impedance modulus of S5 is the smallest, indicating that the corrosion resistance is the worst. The phase angle of S2 is highest in the midfrequency region, suggesting superior capacitive behavior for S2. The phase angles of S1 and S3 in the mid-frequency region are slightly lower than that of S2, while the phase angle of S5 is the lowest in the midfrequency region, indicating that S5 exhibits the weakest capacitive behavior and the poorest corrosion resistance. According to the equivalent circuit fitting parameters listed in Table 3, Q-Yo = 2.999 \times 10 $^{-7}$ of S3 is the minimum value, and Q-n = 0.8353 is closest to 1, indicating

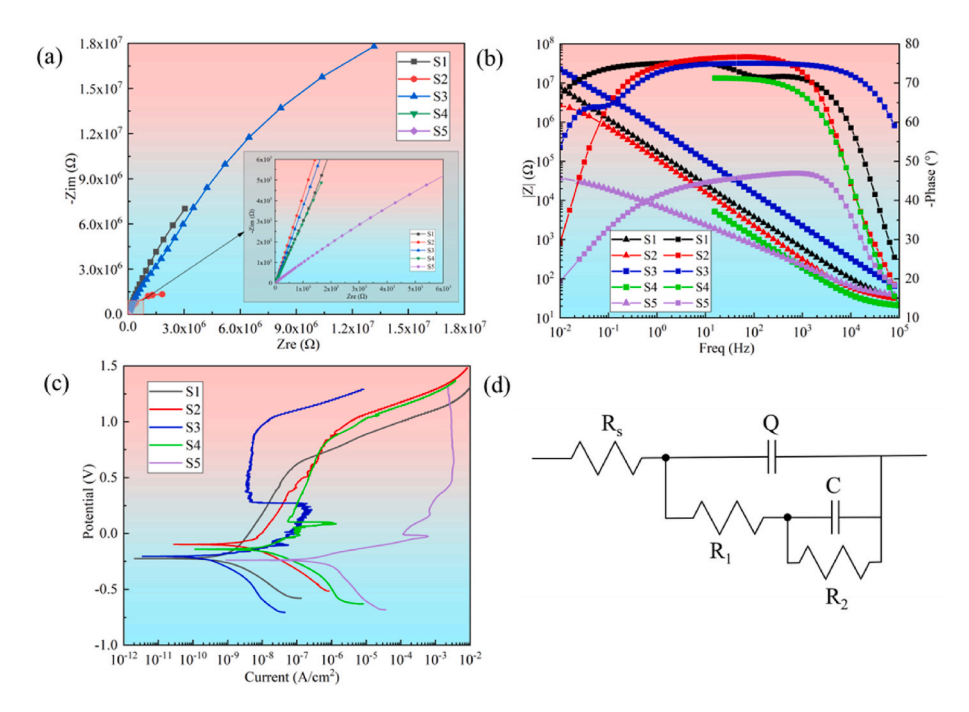


Fig. 11. Electrochemical test diagrams of coatings; (a) Nyquist curve; (b) Bode curve; (c) Polarization curve; (d) equivalent circuit diagram.

 Table 3

 Equivalent circuit fitting parameters of five coatings.

-		•					
No.	R_S	Q-Yo	Q-n	R_1	С	R_2	$\Sigma \chi^2$
	(Ω·cm ²)	(μS·sn/cm ²)		(Ω·cm ²)	(μF/cm ²)	(Ω·cm ²)	10^{-3}
S1	28.46	1.197×10^{-6}	0.8268	4.158×10^4	4.718×10^{-8}	5.134×10^{7}	0.7027
S2	25.50	1.741×10^{-6}	0.8275	9.670×10^{1}	$1.318 imes 10^{-7}$	3.671×10^{6}	1.056
S3	18.67	2.999×10^{-7}	0.8353	1.468×10^{7}	$2.288 imes 10^{-7}$	4.066×10^{7}	1.058
S4	18.10	5.103×10^{-6}	0.7869	8.095×10^{1}	6.575×10^{-8}	7.178×10^{12}	0.277
S5	21.19	4.971×10^{-5}	0.5093	7.767×10^{1}	1.132×10^{-7}	6.095×10^{4}	2.678

that the double-layer capacitance behavior is favorable, which is related to better corrosion resistance. The charge transfer resistance $R_1=1.468\times 10^7$ is the maximum value, indicating that the corrosion rate of the material is the lowest and the corrosion resistance is the best. In addition, the fitting errors $\Sigma\chi^2$ are minimal, indicating a strong fit and reliable data.

Fig. 11(c) presents the potentiodynamic polarization curve. S1 has no obvious passivation zone since no Nb and Ni-coated graphite particles are added. The passivation film of S2 is broken. The passivation zone of S3 is the largest, showing strong corrosion resistance. The passivation zones of S4 and S5 are smaller than that of S3. The electrochemical parameters calculated according to Tafel's law are shown in Table 4. The lowest corrosion current density indicates strong corrosion resistance [31,32]. Among the five coatings, S3 ($i_{corr} = 2.1829E-10$) has the best corrosion resistance, and S5 ($i_{corr} = 4.8077E-7$) has the worst corrosion resistance.

The surface morphology after electrochemical corrosion is shown in

Table 4 Electrochemical parameters of five coatings in 3.5 % NaCl solution.

No.	i _{corr}	E _{corr}	β_a	β_c
	(A/cm ²)	(mV)	(mV)	(mV)
S1	6.8292E-10	-0.2235	229.34	-141.81
S2	2.3791E-09	-0.0786	121.27	-134.36
S3	2.1829E-10	-0.2067	49.136	-146.92
S4	5.8190E-09	-0.1035	56.734	-126.61
S5	4.8077E-07	-0.1969	53.505	-271.08

Fig. 12. A large number of intergranular corrosion pits appear on the surface of S1, and S2 also exhibit intergranular corrosion. In contrast, S3 and S4 primarily show pitting corrosion, while S5 presents both intergranular corrosion and pitting corrosion. According to the standard electrode potentials $\phi Nb3+/Nb = -1.099V$, $\phi Cr3+/Cr = -0.744V$, ϕ Mo3+/Mo = -0.200V, and ϕ Ni2+/Ni = -0.257V, Nb has the lowest potential, so Nb formed a passivation film first and played a major role in the passivation film. As seen from the polarization curve in Fig. 11(c), the passivation region of S3 is the largest, suggesting that its passivation film effectively prevented further corrosion and provided protection across a wider potential range. Despite the addition of more Nb and Nicoated graphite particles to S4 and S5, their corrosion resistance did not improve. This was attributed to the in-situ generation of excess NbC phases, which promoted grain boundary precipitation, thereby reducing corrosion resistance in the electrolyte [33]. Additionally, the excess Nb hindered the formation of passivation films composed of Cr, Mo, and Ni. Scando et al. [34] found that plating with 3 % directly added Nb achieved optimal corrosion resistance, as the corrosion products formed by excessive Nb filled the corrosion pits after dissolution, creating a "blocking effect" that reduced overall corrosion resistance. The electrochemical experiments demonstrated that the fused coatings with 10 % Nb and Ni-coated graphite particles (S3) exhibited the best corrosion resistance with a low degree of surface corrosion. However, a further increase in the content of Nb and Ni-coated graphite particles did not significantly enhance corrosion resistance.

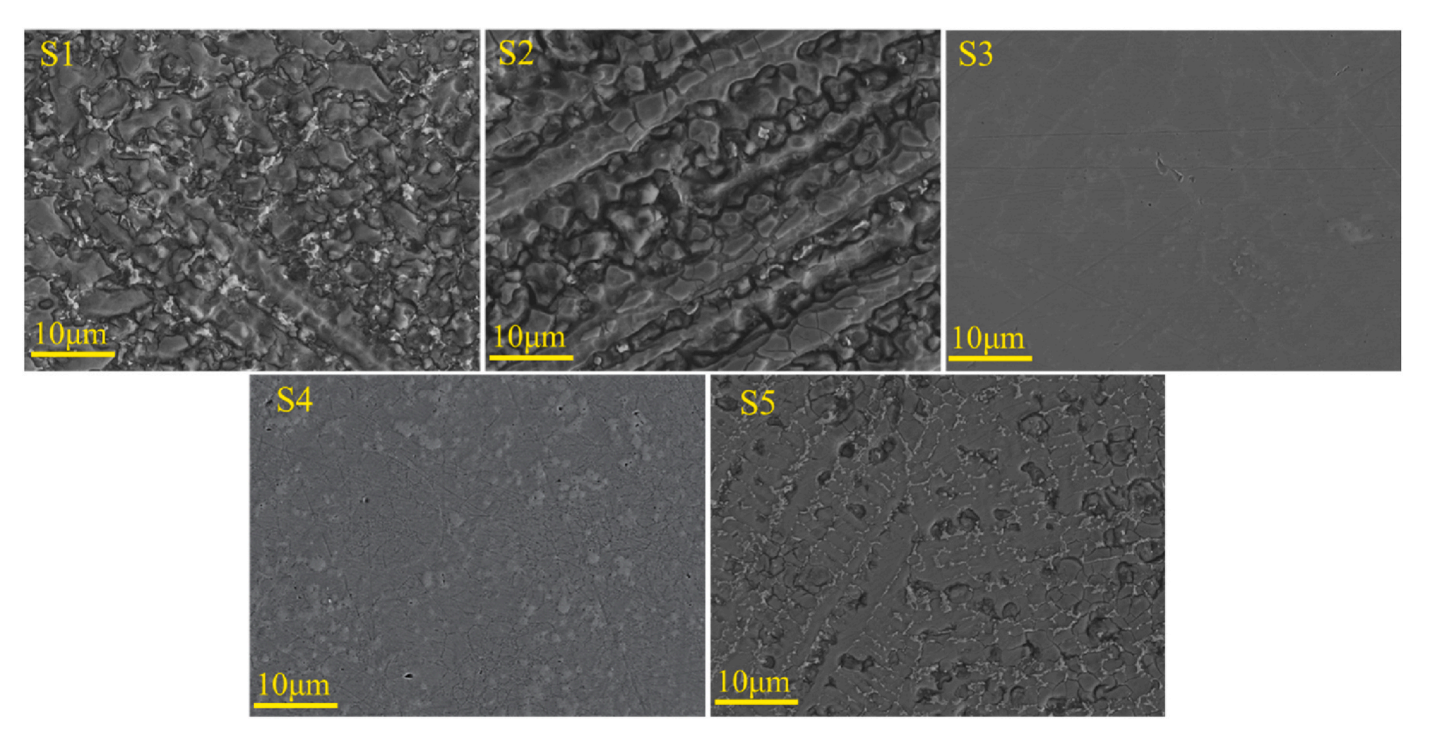


Fig. 12. Electrochemical corrosion morphologies of five coatings.

4. Conclusions

The research objective is to enhance the mechanical properties and corrosion resistance of Ni625 by generating NbC in-situ through the addition of Nb powder and Ni-coated graphite particles, utilizing laser cladding technology. This study demonstrates that an adequate quantity of in-situ generated NbC can significantly improve both the mechanical properties and corrosion resistance of the coating. The specific results are as follows:

- 1. The diffraction peaks of the NbC phase in the 15 % addition coating (S4) show the highest intensity, and EDS analysis confirms that this coating contains the highest Nb content. As the amount of additional material increases, the coating grains progressively refine, and distinct blocky precipitates (NbC) are observed at the grain boundaries. The 20 % addition coating (S5) does not result in the formation of additional in-situ synthesized NbC phases.
- 2. The coating with a 15 % addition (S4) exhibits optimal mechanical properties. It has a hardness of 441.9 HV, which is 1.53 times of the 0 % addition coating (S1). Additionally, its wear coefficient (μ) of the coating is 0.4804, and the wear volume is 0.0042 mm³, representing a reduction of 23.5 % and 64.1 %, respectively, in comparison to the coating with 0 % addition coating (S1). However, the mechanical properties of the 20 % addition coating (S5) did not show any further improvement.
- 3. The 10 % addition coating (S3) exhibits the best corrosion resistance, with the lowest corrosion current density of $2.1829E-10~\text{A/cm}^2$ and a wide passive region, protecting a broad potential range. The corrosion pattern shows slight pitting corrosion. The 15 % addition coating (S4) and the 20 % addition coating (S5) did not exhibit any further improvement in corrosion resistance.

CRediT authorship contribution statement

Yingying Zhang: Writing – review & editing, Writing – original draft, Methodology, Investigation, Data curation. Tianbiao Yu: Supervision, Project administration, Methodology, Funding acquisition. Jiayu Sun: Investigation. Zhengyu Sun: Validation. Yiqi Wang:

Visualization.

Declaration of competing interest

The authors declare that they have no known competing financial interests or personal relationships that could have appeared to influence the work reported in this paper.

Acknowledgment

This work was supported by the National Natural Science Foundation of China [Grant number 52075088], Liaoning Provincial Key Laboratory of Large Equipment Intelligent Design and Manufacturing Technology [Grant number 18006001].

References

- [1] L. Zhu, P. Xue, Q. Lan, G. Meng, Y. Ren, Z. Yang, P. Xu, Z. Liu, Recent research and development status of laser cladding: a review, Opt Laser. Technol. 138 (2021) 106915, https://doi.org/10.1016/j.optlastec.2021.106915.
- [2] Z. Sun, L. Chen, X. Chen, F. Meng, T. Yu, J. Zhao, Analysis and prediction of Cu-Sn-Ti alloy deposited on 316 L steel by coaxial laser cladding, Optik 282 (2023), https://doi.org/10.1016/j.ijleo.2023.170839.
- [3] H. Wang, M. Wu, X. Miao, X. Jin, C. Cui, C. Ma, Q. Wang, Effect of Nb on the microstructure and wear resistance of In625/(Nbx+SiC0.5) composite coatings by laser cladding, Ceram. Int. 49 (2023) 38420–38431, https://doi.org/10.1016/j. ceramint.2023.09.247.
- [4] Y. Chenglong, L. Yuling, K. Dejun, Laser cladded Ni625–xCr3C2 coatings: microstructure, tribocorrosion and electrochemical properties, Surf. Coating. Technol. 478 (2024) 130487, https://doi.org/10.1016/j.surfcoat.2024.130487.
- [5] J. Huebner, D. Kata, J. Kusiński, P. Rutkowski, J. Lis, Microstructure of laser cladded carbide reinforced Inconel 625 alloy for turbine blade application, Ceram. Int. 43 (2017) 8677–8684. https://doi.org/10.1016/j.ceramint.2017.03.194.
- [6] Y. Chenglong, K. Dejun, Microstructure, tribocorrosion and corrosion performances of laser cladded Ni625-xTiC coatings in 3.5% NaCl solution, J. Therm. Spray Technol. 33 (2024) 260–274, https://doi.org/10.1007/s11666-024-01717-3.
- [7] P. Xuelong, F. Hanguang, S. Shuting, L. Jian, L. Yongping, W. Wenbo, Z. Jianxin, Effect of Nb addition on microstructure and properties of laser cladding NiCrBSi coatings, Trans. Inst. Metal Finish. 96 (2018) 304–312, https://doi.org/10.1080/ 00202967 2018 1502934
- [8] H. Zhang, Y. Zhang, Q. Cao, Y. Pan, G. Lian, L. Que, X. Zhu, A comparative investigation on microstructure evolution and wear resistance of in situ synthesized NbC, WC, TaC reinforced Mo2FeB2 coatings by laser cladding, Ceram. Int. 49 (2023) 894–906, https://doi.org/10.1016/j.ceramint.2022.09.064.

- [9] Y. Liu, K. Wang, H. Fu, X. Yang, J. Lin, Effect of NbC addition on the microstructure and wear resistance of laser cladding nickel-based alloy coatings, J. Mater. Eng. Perform. (2023), https://doi.org/10.1007/s11665-023-08828-y.
- [10] L.H.R. Apolinário, E.A. Torres, H.R. Araújo, A.D.A. Vicente, T.F.D.A. Santos, Effect of laser cladding parameters in NbC reinforced 316L austenitic stainless steel composite depositions on a mild steel, Int. J. Adv. Manuf. Technol. 122 (7–8) (2022) 3095–3113. https://10.1007/s00170-022-10067-9.
- [11] Q. Cheng, H. Chen, Y. Hou, L. Fan, L. Dong, Y. Yin, Wear and corrosion properties of plasma transferred arc Ni-based coatings reinforced with NbC particles, Mater. Sci. 27 (2021) 294–301, https://doi.org/10.5755/j02.ms.24211.
- [12] S. Yufan, F. Hanguang, P. Xuelong, S. Shuting, L. Jian, L. Yongping, Effect of process parameters and niobium carbide addition on microstructure and wear resistance of laser cladding nickel-based alloy coatings, Mater. Werkst. 51 (2020) 54-65, https://doi.org/10.1002/mawe.201800221.
- [13] L. Chen, Y. Chen, X. Chen, T. Yu, Z. Wang, Microstructure and properties of in situ TiC/Ni functionally gradient coatings by powder-fed laser cladding, Ceram. Int. 48 (2022) 36789–36801, https://doi.org/10.1016/j.ceramint.2022.08.243.
- [14] Q. Wu, W. Long, L. Zhang, H. Zhao, A review on ceramic coatings prepared by laser cladding technology, Opt Laser. Technol. 176 (2024) 110993. https://10.1016/j. optlaster 2024 110993
- [15] H.F. Zhang, S. Zhang, H. Wu, R. Wang, C.H. Zhang, C.L. Wu, J. Chen, H.T. Chen, Mechanical properties and corrosion resistance of laser cladding iron-based coatings with two types of NbC reinforcement, Surf. Coat. Technol. 479 (2024) 130558, https://doi.org/10.1016/j.surfcoat.2024.130558.
- [16] C. Zhang, W. Sun, E. Liu, Y. Liu, J. Liu, B. Zhang, M. Zhou, Y. Xu, Effects of process parameters on microstructure and properties of in-situ synthesized WC-reinforced Ni-based cladding layer, Mater. Res. 27 (2024). https://10.1590/1980-5373-mr-2023-0572
- [17] W. Xi, B. Song, Z. Sun, T. Yu, J. Wang, Q. Sun, Effect of various morphology of in situ generated NbC particles on the wear resistance of Fe-based cladding, Ceram. Int. 49 (2023) 10265–10272, https://doi.org/10.1016/j.ceramint.2022.11.206.
- [18] B. Shi, S. Huang, P. Zhu, C. Xu, T. Zhang, Microstructure and wear behavior of insitu NbC reinforced composite coatings, Materials 13 (2020) 3459, https://doi.org/ 10.3390/ma13163459.
- [19] Y. Liu, K. Wang, H. Fu, B. Zong, J. Zhang, Wear resistance of in situ NbC-reinforced laser cladding Ni45 coatings, Lubricants 11 (2023) 316, https://doi.org/10.3390/ lubricants 11080316
- [20] Z. Wang, J. Ni, Y. Bian, X. Li, Y. Shao, Y. Song, X. Hao, Y. Xu, J. Ye, L. Luo, Enhancement of in-situ NbC oxidation with size reduction and its effect on electrochemical corrosion resistance of Cu-matrix composites, Ceram. Int. 49 (2023) 37040–37045. https://doi.org/10.1016/j.ceramint.2023.08.265.
- [21] Y. Zhao, L. Chen, J. Sun, W. Wu, T. Yu, Microstructure evolution and wear resistance of in-situ synthesized (TI, Nb)C ceramic reinforced Ni204 composite coatings, Ceram. Int. 48 (2022) 17518–17528, https://doi.org/10.1016/j. ceramint.2022.03.016.

- [22] H. Zhang, Y. Zhang, Q. Cao, Y. Pan, G. Lian, L. Que, X. Zhu, A comparative investigation on microstructure evolution and wear resistance of in situ synthesized NbC, WC, TaC reinforced Mo2FeB2 coatings by laser cladding, Ceram. Int. 49 (2023) 894–906, https://doi.org/10.1016/j.ceramint.2022.09.064.
- [23] G. Lian, K. Yue, C. Chen, L. Huang, M. Zheng, Influences of powder ratios on the mechanical properties of in-situ synthetic NbC coatings, Mater. Today Commun. 35 (2023) 106318, https://doi.org/10.1016/j.mtcomm.2023.106318.
- [24] L. Chen, T. Yu, P. Xu, B. Zhang, In-situ NbC reinforced Fe-based coating by laser cladding: simulation and experiment, Surf. Coating. Technol. 412 (2021) 127027, https://doi.org/10.1016/j.surfcoat.2021.127027.
- [25] S. Gaddam, M.S.K.K. Nartu, A. Chesetti, S.A. Mantri, R.S. Mishra, N.B. Dahotre, R. Banerjee, Hierarchical phase evolution during direct laser deposition of an insitu Ni-NbC composite, Scripta Mater. 226 (2023) 115225, https://doi.org/ 10.1016/j.scriptamat.2022.115225.
- [26] R. Wang, C. Ouyang, Q. Li, Q. Bai, C. Zhao, Y. Liu, Study of the microstructure and corrosion properties of a Ni-based alloy coating deposited onto the surface of ductile cast iron using high-speed laser cladding, Materials 15 (5) (2022). https:// 10.3390/ma15051643.
- [27] F. Liang, K. Li, W. Shi, Z. Zhu, Effect of Y2O3 content on microstructure and corrosion properties of laser cladding Ni-based/WC composite coated on 316L substrate, Coatings 13 (9) (2023) 1532. https://10.3390/coatings13091532.
- [28] J. Wang, X. Cui, G. Jin, Y. Zhao, X. Wen, Y. Zhang, Effect of in-situ Ni interlayer on the microstructure and corrosion resistance of underwater wet 316L stainless steel laser cladding layer, Surf. Coating. Technol. 458 (2023) 129341. https://10.101 6/i.surfcoat.2023.129341.
- [29] K. Yao, L. Zongde, L. Quanbing, Effect of laser power on microstructure and properties of Ni-based alloy coatings on 30CrMnSiA steel, J. Therm. Spray Technol. 31 (7) (2022) 2136–2146. https://10.1007/s11666-022-01416-x.
- [30] H. Zhang, Y. Zhang, Q. Cao, Y. Pan, G. Lian, L. Que, X. Zhu, A comparative investigation on microstructure evolution and wear resistance of in situ synthesized NbC, WC, TaC reinforced Mo2FeB2 coatings by laser cladding, Ceram. Int. 49 (2023) 894–906, https://doi.org/10.1016/j.ceramint.2022.09.064.
- [31] L. Guo, F. Xiao, F. Wang, Y. He, W. Wei, Y. Zhang, Microstructure and corrosion resistance of inconel 625 overlay welded by pulsed TIG process, Int. J. Electrochem. Sci. 16 (2021) 210418, https://doi.org/10.20964/2021.04.11.
- [32] M. Scendo, K. Staszewska-Samson, H. Danielewski, Corrosion behavior of inconel 625 coating produced by laser cladding, Coatings 11 (2021) 759, https://doi.org/ 10.3390/coatings11070759.
- [33] G. Jie, M. Qingchao, S. Yan, W. Kangning, S. Qiang, W. Canming, Effect of Nb content on microstructure and corrosion resistance of Inconel 625 coating formed by laser cladding, Surf. Coat. Technol. 458 (2023) 129311, https://doi.org/10.1016/j.surf.coat.2023.129311.
- [34] M. Scendo, S. Spadlo, K. Staszewska-Samson, P. Mlynarczyk, Influence of heat treatment on the corrosion resistance of aluminum-copper coating, Metals 10 (2020) 966, https://doi.org/10.3390/met10070966.